Grain boundary mediated plasticity in aluminum films unraveled by a statistical approach combining nano-DIC and ACOM-TEM

Supplementary material

Paul BARAL [1,2,†], Ankush KASHIWAR [1,3,†], Michaël COULOMBIER [1], Laurent DELANNAY [1], Khalid Hoummada [4], Jean Pierre RASKIN [5], Hosni IDRISSI [1,3], Thomas PARDOEN [1,6]*

(1) Institute of Mechanics, Materials and Civil Engineering (IMMC), UCLouvain, B-1348, Louvain-la-Neuve, Belgium

(2) Univ. Lyon, Mines Saint Etienne, CNRS UMR 5307 LGF, Centre SMS, 42100 Saint Etienne, France

(3) EMAT, University of Antwerp, Groenenborgerlaan 171, B-2020, Antwerp, Belgium

(4) IM2NP, Aix Marseille Univ/CNRS, UMR 7334, 13397 Marseille, France

(5) Institute of Information and Communication Technologies, Electronics and Applied Mathematics (ICTEAM), UCLouvain, B-1348, Louvain-la-Neuve, Belgium

(6) WEL Research Institute, avenue Pasteur 6, B-1300, Wavre, Belgium

* Corresponding author: thomas.pardoen@uclouvain.be

[†]Paul Baral and Ankush Kashiwar should be considered as co-first authors. Both authors have equally contributed to the work.

1. Sample summary

Table S1 Summary of Al specimens described in the study.

Specimen	Macro strain	Characterization
TOC 0	0.000	ACOM TEM
TOC 04	0.023	nano-DIC
TOC 08	0.038	nano-DIC
TOC 14	0.059	nano-DIC
TOC 32	0.122	nano-DIC
TOC 46	0.165	nano-DIC / ACOM TEM

2. Chemical characterization of the aluminum film

Atom probe tomography (APT) was used to check the purity of the Al films used in the present work (see Figure S1 below). The results obtained on several tips did not reveal the presence of impurities. However, it should be noted that the investigation of GBs was not possible due to the difficulty to detect the boundaries in the tip. Further experiments involving preliminary TEM observations prior to APT analysis are needed to investigate the purity of GBs and the possible link with the GB processes reported in the present study.

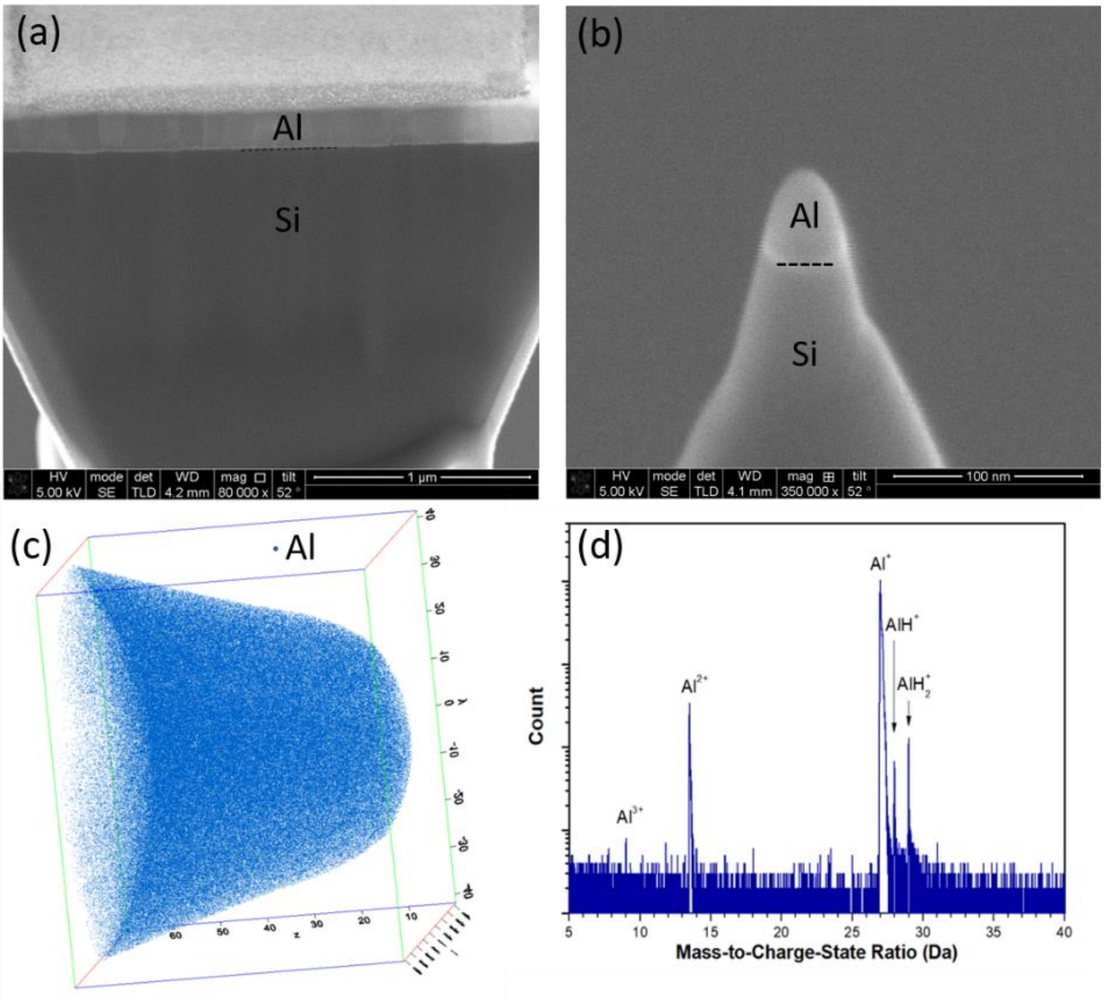

Figure S1 Atom probe tomography results obtained on Al thin film deposited on silicon. (a) SEM image of the Al thin film. Grain boundaries can be observed in this image. (b) SEM image of the final needle-shaped tip containing Al thin film at the top of the tip. Theses APT tips were prepared with a dual-beam (SEM/FIB) system after the deposition of a protective layer of Pt. (c) 3D reconstructed volume obtained by APT showing the distribution of Al atoms. This volume corresponds to the tip surface in (b). (d) The analysis of the mass spectrum of this APT volume shows the presence of only Al atoms.

3. Nano-particles distribution

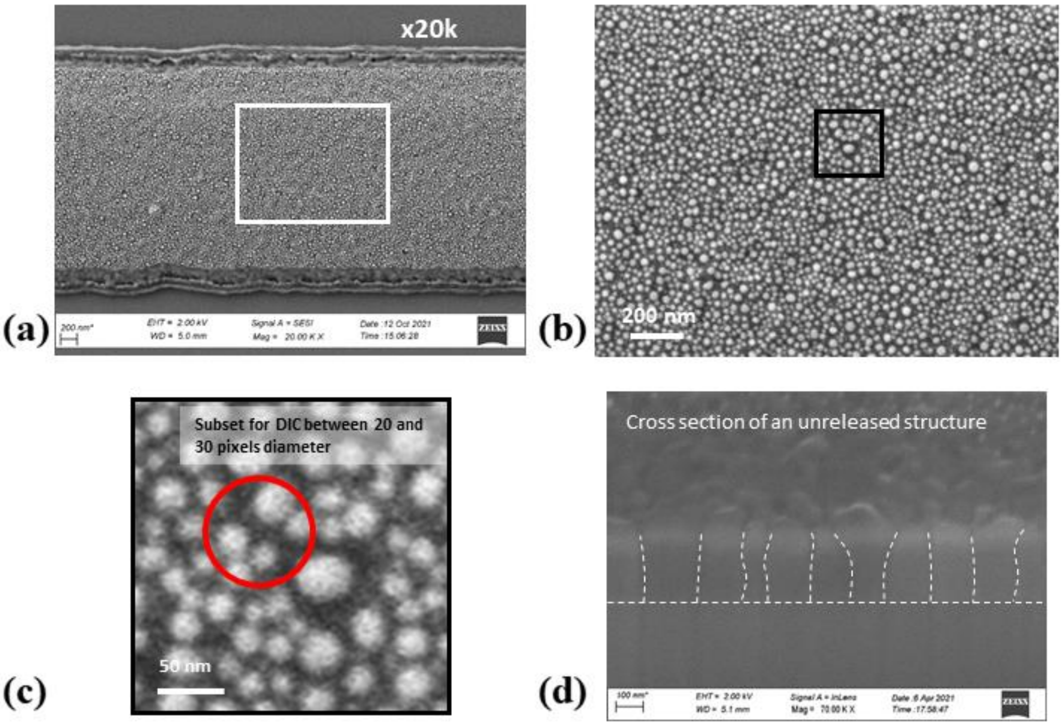

Figure S2 Indium nano-particles deposition : a) top view of a specimen after deposition of indium nano-particles, b) zoomed view of the pattern, c) dimension of the subset used for correlation (red circle) and d) cross section of a Al specimen showing the columnar growth in the thickness of the film.

Distribution of indium nano-particles have been estimated from a 50 kx magnification image of the sample surface in a SEM. The image has been binarized with Matlab in order to obtain particles radius. The distribution is fitted with a gaussian, with an average radius of 8.1 nm.

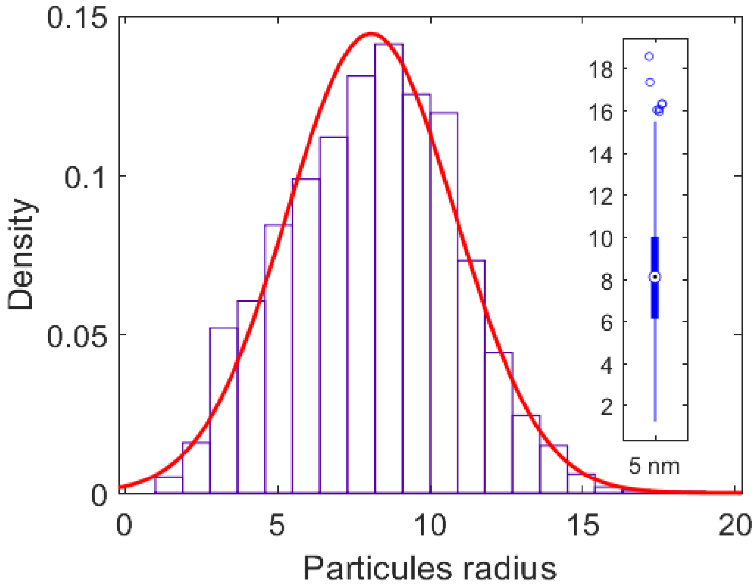

Figure S3 Indium nano-particle size distribution.

4. Through-thickness microstructure

Figure S4.a and b shows the crystal orientation maps along the film growth direction which were acquired from both sides of the film. Both the maps show similar shapes of the grains and crystal orientation. Also, a 3D-like analysis of the grain boundaries through the film thickness is achieved in the correlation coefficient map of Fig. S4.c. No contrast changes are visible within most of the grains, except for a few where the contrast changes result from the presence of dislocations or subgrain boundaries. Therefore, all the maps shown in Fig. S4 support the fact that individual grains pass through the thickness of the specimen, and that there are no (or almost no) overlapping grains.

The map shows a majority of the grain boundaries with sharp contrast indicating that they are almost parallel to the film growth direction while some of them exhibit small inclination. The maximum inclination measured from the projections in the correlation coefficient maps is about 14° (calculated by dividing the distance between the two projections of one of the highest tilted GB by the film thickness, as highlighted in Fig. S4.c). Hence, the inclination of the grain boundaries ranges from 0° to 14°.

Based on these measurements, the out-of-plane grain boundary resolved shear stress (GBRSS) ranges from 0 to 0.23. The grains would therefore preferentially slide in the out-of-plane direction if the in-plane GBRSS is less than the out-of-plane. From the distribution of in-plane GBRSS, calculated on the deformed sample, the percentage of GB with GBRSS larger than 0.23 is 78 %. It is therefore easier for a majority of the grains to rotate in plane rather than out-of-plane. Moreover, the film thickness is 240 nm and a majority of the grains are below 200 nm in equivalent diameter (see Fig. 6 in the manuscript). The geometrical constraint on the grains should not promote the out-of-plane grain rotation. This has been also observed and explained by J.P. Liebig (reference [24] in the manuscript).

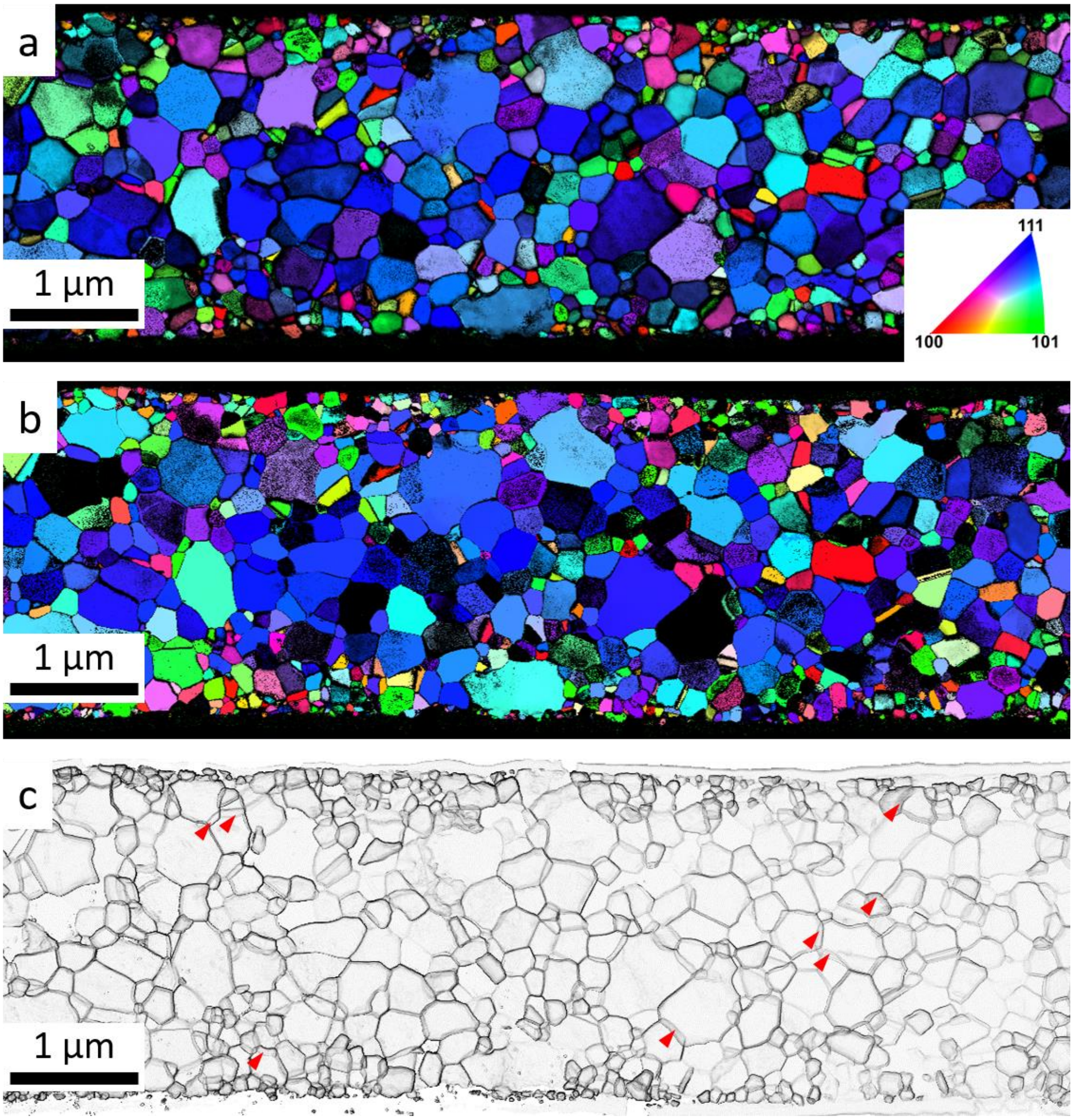

Figure S4 Crystal orientation maps along the film growth direction acquired from the film: a) upper surface on top, b) lower surface on top and c) correlation coefficient map with red markers showing the projection effects from grain boundaries.

5. Strain hardening

Figure S5 shows the engineering stress as a function of the plastic strain for the aluminum thin films. An Hollomon hardening law (in the form of $\sigma_y + A\left(\epsilon_p\right)^n$) is fitted to the data to obtain the hardening exponent $n = 0.14$. Considering the long elasto-plastic transition, from 100 to 200 MPa, it is difficult to state were to consider the pure plastic regime. Therefore, the fit is not very representative ($R^2 = 0.69$) and the 95 % confidence interval is given to be $A \in [152{,}223]\ MPa$ and $n \in [0.07{,}0.20]$.

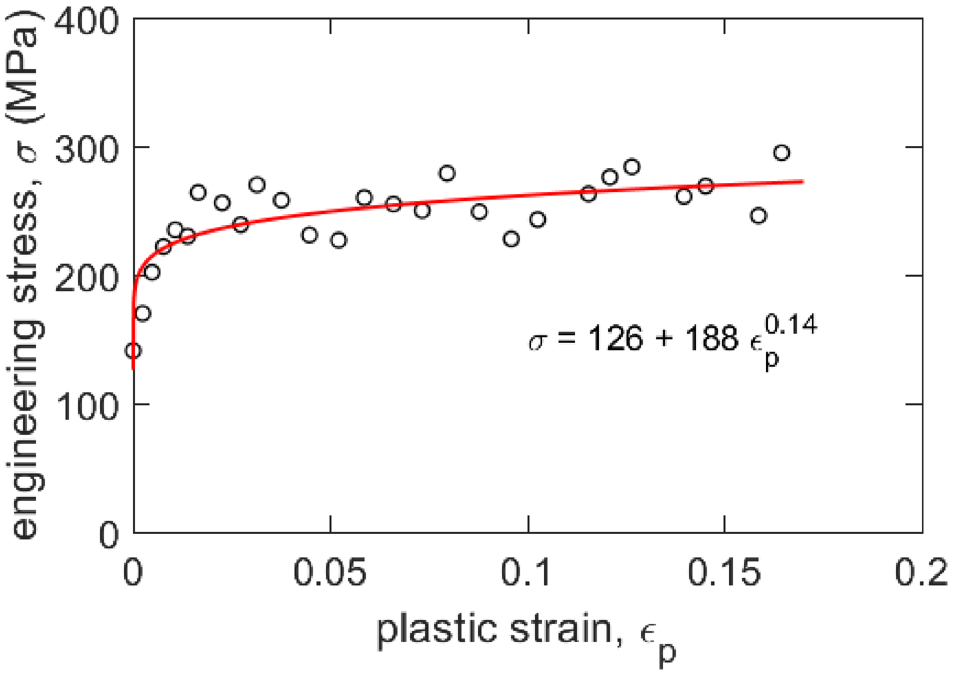

Figure S5 Engineering stress as a function of the plastic strain, fitted with a Hollomon hardening law.

6. Strain rate sensitivity

Creep/relaxation measurements, using the tensile on-chip technique [62], provide an average strain rate sensitivity exponent $m = 0.05 \pm 0.02$, assuming that the yield stress is linked to the strain rate according to a simple power law $\sigma = K\,\dot{\epsilon}^{m}$. This rate sensitivity is determined based on the progressive relaxation of the stress in nine specimens deformed between 0.012 and 0.043 macro-strain. The stress and strain state of the specimens are measured after the release of the structures at three times (around 1h, 2 days and 7 days after release). The three measurements are used to compute two strain rates by a numerical differential. The results of the calculated stress and strain rate pairs for each specimen are shown in Fig. S6 and Table S2 compile the calculated strain rate sensitivity exponents.

Table S2 Strain rate sensitivity exponent and initial strain, after release, calculated from relaxation measurements.

Sample Name	TOC 12	TOC 14	TOC 16	TOC 18	TOC 20	TOC 24	TOC 26	TOC 28	TOC 30
Initial strain ϵ^{∞}	0.0115	0.0144	0.0173	0.0204	0.0230	0.0290	0.0335	0.0375	0.0434
m	0.028	0.047	0.090	0.069	0.076	0.023	0.039	0.031	0.034

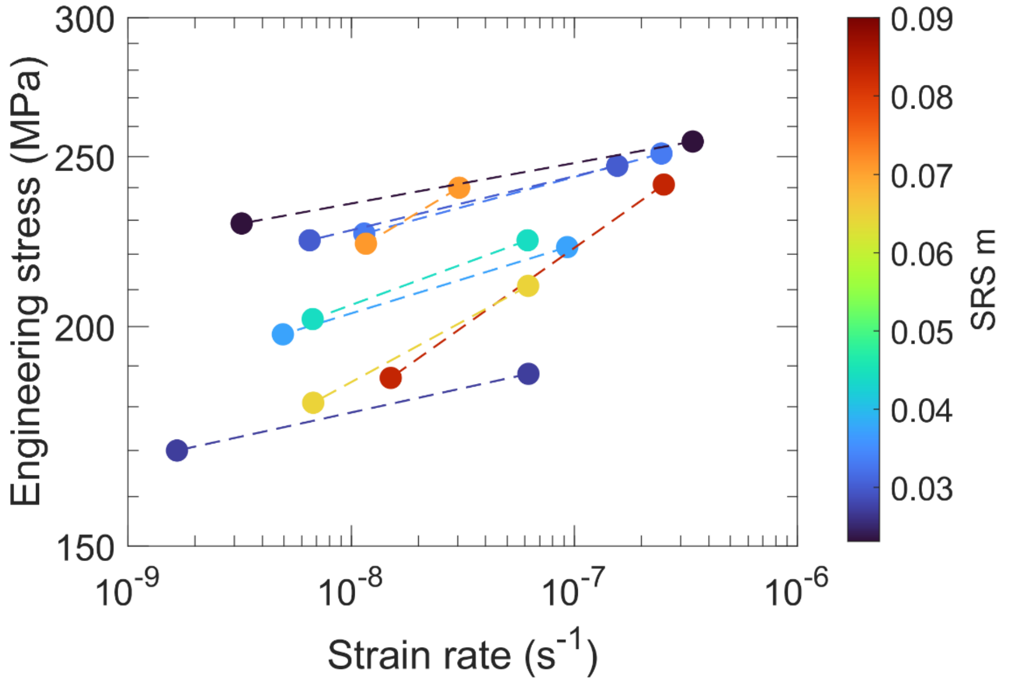

Figure S6 Engineering stress as a function of strain rate for 9 tensile specimen deformed between 0.015 and 0.043. The color bar shows the strain rate sensitivity exponent m.

7. Grain rotation in TOC32

The entire observed region in sample TOC32 used to compute the cluster size as a function of cluster rotation amplitude is shown in Fig. S7. The moderately deformed regions ($\epsilon_{VM} < 0.18$) are individualized as clusters and the rotation field ω_{xy} in each of them is represented in Fig. S5.a. Clusters are assumed to undergo uniform rotation if the average ω_{xy} value is larger than 1.5 times its standard deviation. Fig. S7.b represents clusters satisfying this condition.

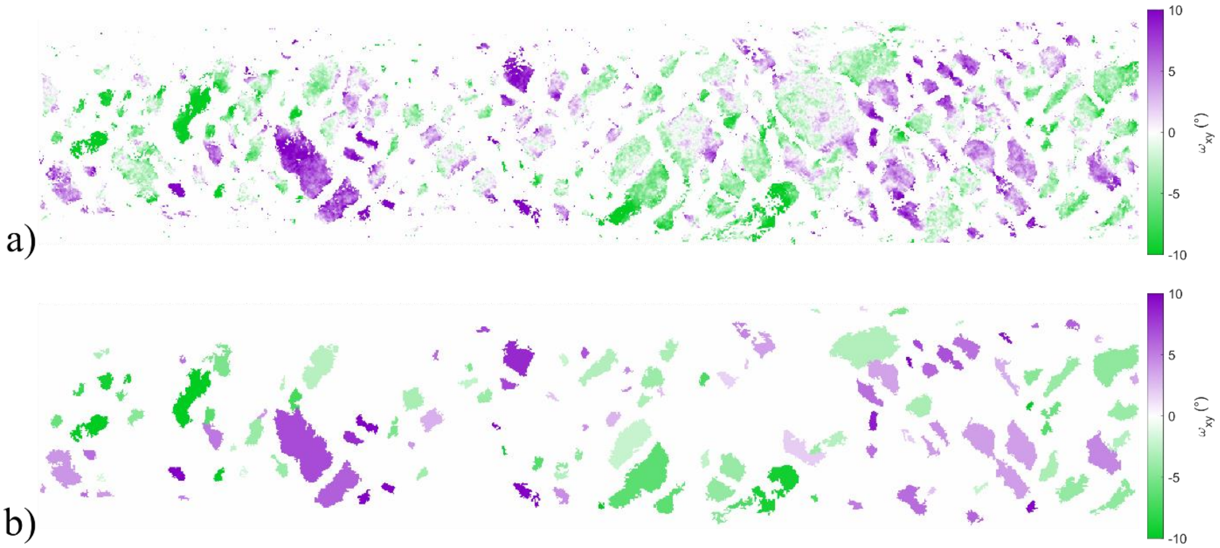

Figure S7 Rotation component of the transformation: a) as calculated rotation for low deformation clusters ($\epsilon_{VM} < 0.18$) and b) average rotation per cluster, only homogeneous rotation of the clusters are considered.

8. Grain size distribution along the width of the sample

Distribution of grain size as a function of the position along the width of the sample have been estimated by cutting the width of the beam in 7 equal segments (see blue dashed lines in Fig. S8). If the centroid of the grain (see red markers in Fig. S6) is located within one segment, the associated grain size is allocated to the segment.

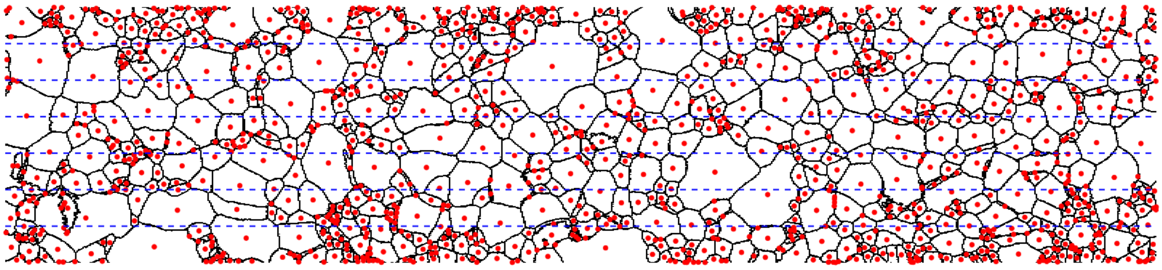

Figure S8 Microstructure of the deformed Al sample. The red markers represent the centroid of each grain and the dashed blue lines represent the segments used to evaluate the distribution of grain size as a function of the beam width.

The results obtained for undeformed and deformed samples are given in Fig. S9. Two observations can be done:

- For both samples, grains are larger at the center of the beam than at the edges.
- There is a clear grain growth after deformation, which is mainly exhibited in the center of the beam.

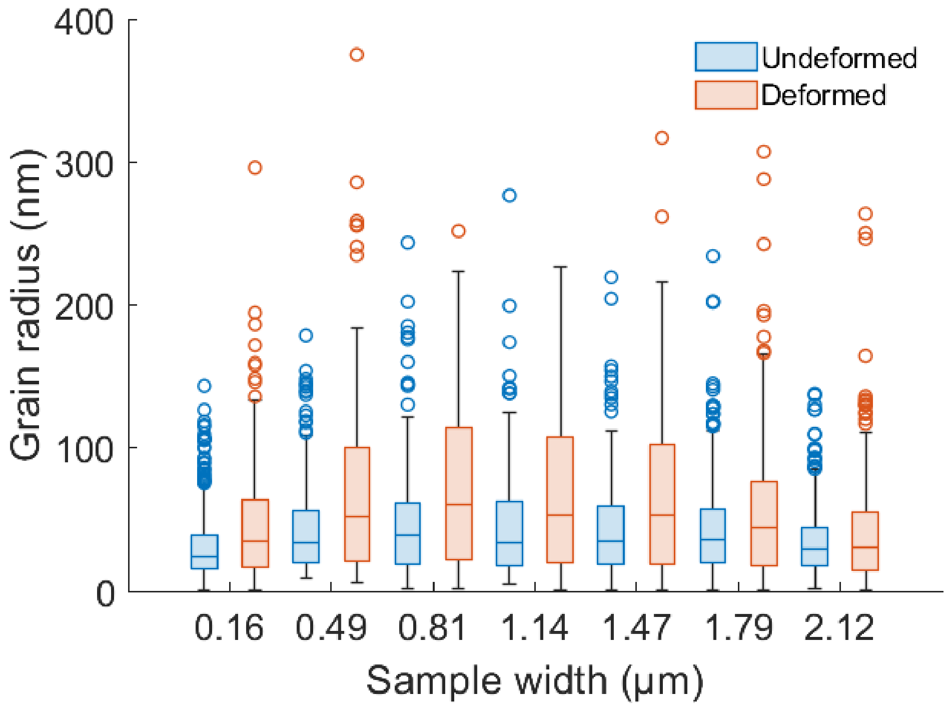

Figure S9 Statistics of grain size as a function of their positon in the width of the sample and as a function of the deformation. The boxes represent the 25th and 75th quartile, the middle line represents the median, the whiskers represent the maximum and minimum without taking into account outliers and open circles are labelled as outliers.

9. Comparison of DIC and TEM: scaling

The scaling of the DIC data obtained with SEM and the microstructure obtained by TEM is done by selecting remarkable artefacts on both images that are very likely to coincide (see Fig. S10). For simplification, we assumed that both observations were made close to horizontal and therefore only a scaling between the two images were done (no rigid body rotation has been introduce to compensate the differences).

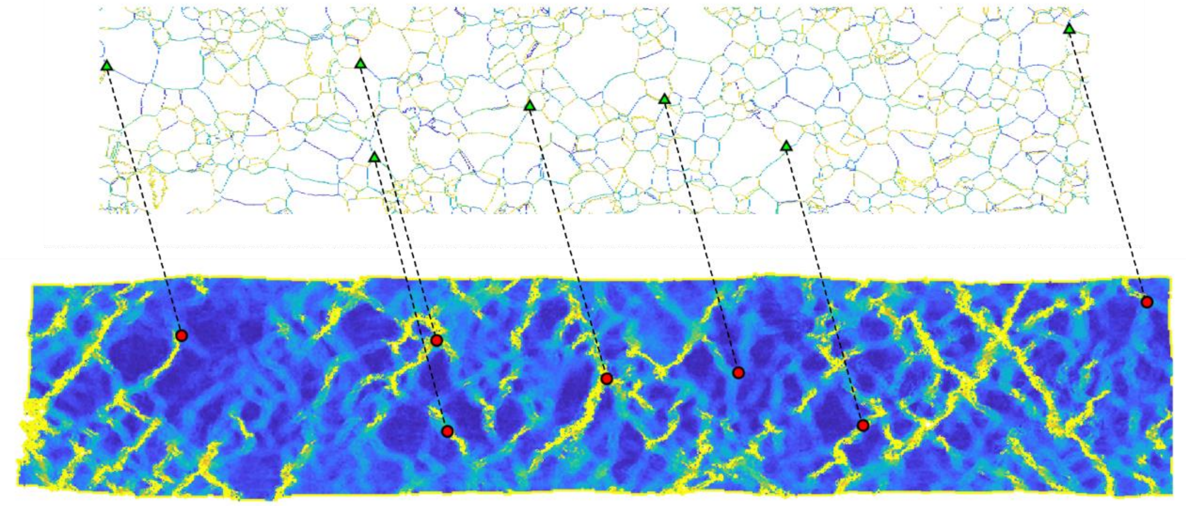

Figure S10 Selection of remarkable points to scale the two images and superimpose the microstructures.

10. Distribution of local strain

In order to evaluate the average local strain within the grain boundaries, a mask of the GB microstructure is removed from the strain map and the average in and out of the mask are performed. Since the spatial resolution of nano-DIC is approximately 50 times the TEM microstructure (1 nm), the GB mask is dilated to measure the variation of average strain with the thickness of the GB. Fig. S11.a represents the portion of pixels attributed to GB or grain as a function of the GB width (GB proportion tends to 0 when width tends to 0). The intersection of the two curves represent the instant where there is as much as pixel in the GB and in the grain (which is not representative of the nearly 1D GB character in the plane). Fig. S11.b represents the average local strain inside and outside the GB. First, the averages strain is always larger within the GB than outside, highlighting the predominant GB plasticity. Average strain in the GB is systematically between 24 and 29 % higher than in the grains, if we consider GB width representative of the microstructure (between 6 and 20 nm width).

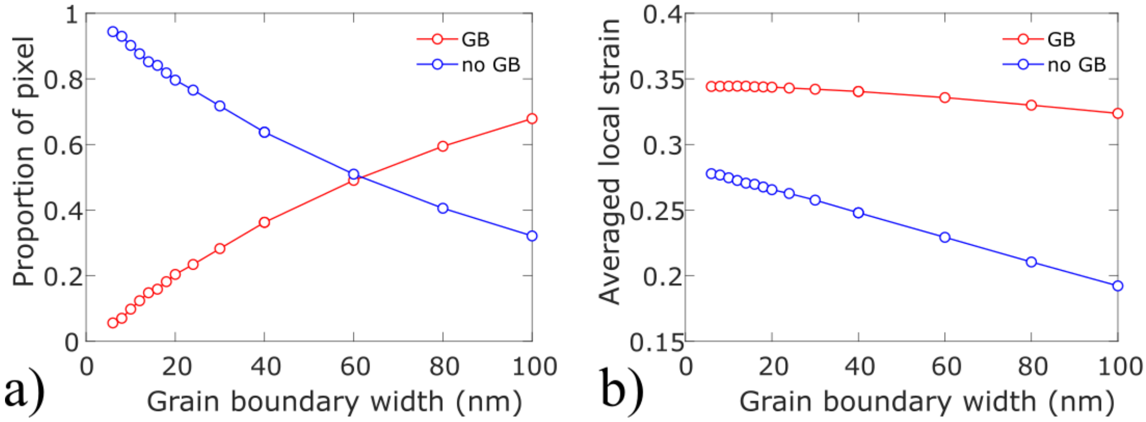

Figure S11 Proportion of GB in the sample and average local strain, as a function of the GB width.

11. Evidences of disconnections

BFTEM imaging was carried in zone 1 to present the evidence for disconnections. In order to confirm the presence of disconnections the images were acquired over various tilt angles as shown in Fig. S12. The disconnections are indicated with arrows show most prominent contrast in Fig. S12.a whereas the contrast becomes weaker with progressive tilting in Fig. S12.b-d. Fig. S13.a shows the disconnections from a triple junction in zone 1 and Fig. S13.b shows disconnections at a GB in zone 3.

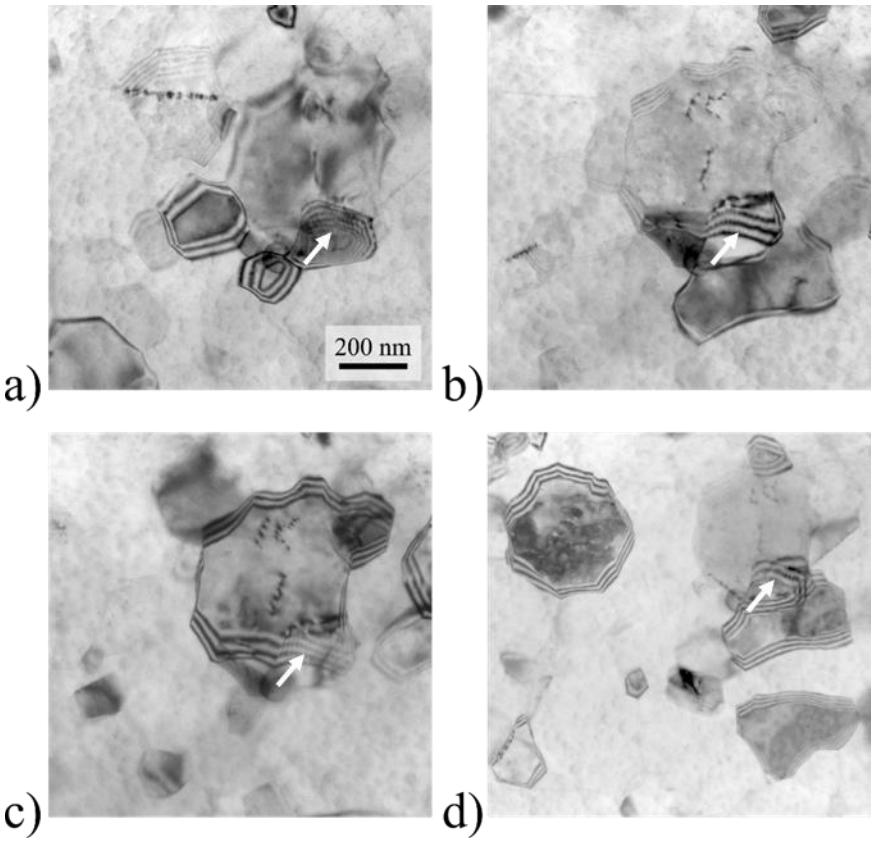

Figure S12 Tilted BF TEM observations of region 1 at : (a) α = -14.3°, β = 8°, (b) α = 6.6°, β = 8°, (c) α = 9.2°, β = 10°,(d) α = -7.5°, β = 14°.

Other grains presenting disconnections at GB.

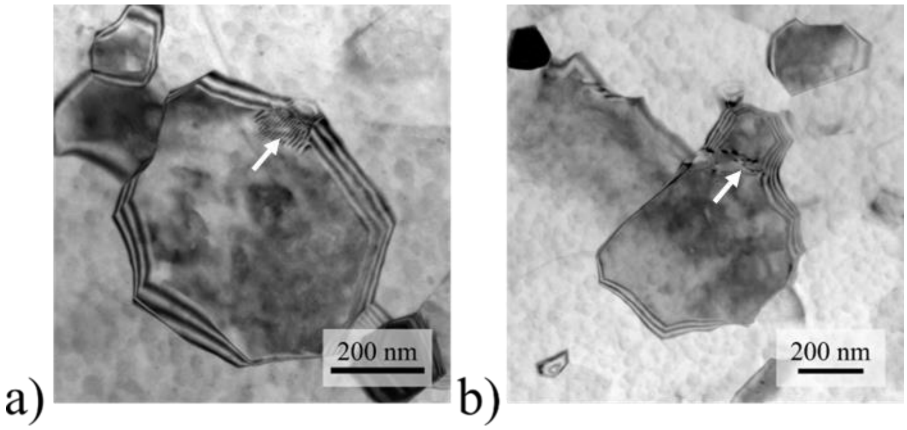

Figure S13 Evidence of disconnections at: (a) GB triple junction in zone 1, (b) GB in zone 3.